communications medicine

A Nature Portfolio journal

Article

https://doi.org/10.1038/s43856-025-00753-6

An axis-specific mitral annuloplasty ring eliminates mitral regurgitation allowing mitral annular motion in an ovine model

Yuanjia Zhu[1,2], Annabel M. Imbrie-Moore[2,3], Matthew H. Park[2,3], Tyler E. Cork[1,4], Shin Yajima[2,5], Robert J. Wilkerson[2], Nicholas A. Tran[2], Mateo Marin-Cuartas[2,6], Danielle M. Mullis[2], Sam W. Baker[7], Yuko Tada[8], Tsuyoshi Ueyama[8], Matthew Leipzig[2], Vicky Y. Wang[4], Sidarth Ethiraj[2], Sarah Madira[2], Shreya Anilkumar[2], Sabrina K. Walsh[2], Haley J. Lucian[2], Chris Huynh[2], Kimberly Morris[2], Ok S. Kim[2], Jack Mulligan[2], Hanjay Wang[2], Yasuhiro Shudo[2], Daniel B. Ennis[4] & Y. Joseph Woo[1,2]

Abstract

Introduction Current mitral annuloplasty rings fail to restrict the anteroposterior distance while allowing dynamic mitral annular changes. We designed and manufactured a mitral annuloplasty ring that demonstrated axis-specific, selective flexibility to meet this clinical need. The objectives were to evaluate ex vivo biomechanics of this ring and to validate the annular dynamics and safety after ring implantation in vivo.

Methods Healthy human mitral annuli ($n = 3$) were tracked, and motions were isolated. Using the imaging data, we designed and manufactured our axis-specific mitral annuloplasty ring. An ex vivo annular dilation model was used to compare hemodynamics and chordal forces after repair using the axis-specific, rigid, and flexible rings in five porcine mitral valves. In vivo, axis-specific ($n = 6$), rigid ($n = 6$), or flexible rings ($n = 6$) were implanted into male Dorset sheep for annular motion analyses. Five additional animals receiving axis-specific rings survived for up to 6 months.

Results Here we show the axis-specific, rigid, and flexible rings reduced regurgitation fraction to 4.7 ± 2.7%, 2.4 ± 3.2%, and 17.8 ± 10.0%, respectively. The axis-specific ring demonstrated lower average forces compared to the rigid ring ($p = 0.046$). Five animals receiving axis-specific rings survived for up to 6 months, with mitral annular motion preserved in vivo. Mature neoendocardial tissue coverage over the device was found to be complete with full endothelialization in all animals.

Conclusions The axis-specific mitral annuloplasty ring we designed demonstrates excellent capability to repair mitral regurgitation while facilitating dynamic mitral annular motion. This ring has tremendous potential for clinical translatability, representing a promising surgical solution for mitral regurgitation.

Plain language summary

If a person has a leaky heart valve and it remains untreated, it can lead to death. One treatment is to insert a special type of ring called an annuloplasty ring around the heart valve to prevent leakage. We designed and manufactured an annuloplasty ring and tested its effectiveness in a heart simulator and in sheep. We found that our ring was able to reduce leakage from the heart valve, while preserving the natural movement of the part of the heart where it was implanted. Our annuloplasty ring could potentially be used in the future to improve the treatment of people with leaky heart valves.

Mitral valve regurgitation (MR) is one of the most prevalent forms of valvular heart disease in Western countries[1,2]. It is estimated to affect up to 19% of the general population in the United States[3] and is a major cause of global morbidity and mortality[4]. The annual US healthcare expenditure on mitral valvular diseases alone was reported to be $13.2 billion, representing the largest aggregate cost among all valvular heart diseases[5]. MR can be caused by various intrinsic lesions of the mitral valve (MV) apparatus[6] and may also result from primary myocardial diseases[7]. Among these lesions,

[1]Department of Bioengineering, Stanford University, Stanford, CA, USA. [2]Department of Cardiothoracic Surgery, Stanford University, Stanford, CA, USA. [3]Department of Mechanical Engineering, Stanford University, Stanford, CA, USA. [4]Department of Radiology, Stanford University, Stanford, CA, USA. [5]Department of Cardiovascular Surgery, Osaka University Graduate School of Medicine, Osaka, Japan. [6]University Department of Cardiac Surgery, Leipzig Heart Center, Leipzig, Germany. [7]Department of Comparative Medicine, Stanford University, Stanford, CA, USA. [8]Stanford Cardiovascular Institute and Division of Cardiovascular Medicine, Stanford University, Stanford, CA, USA. e-mail: joswoo@stanford.edu

mitral annular dilation is one of the most common features of MR with the anteroposterior diameter being greater than the transverse diameter, reversed from the relationship observed in a normal annulus in systole.

MV surgical intervention is the current gold standard for patients with severe symptomatic MR[7,8]. Synthetic mitral annuloplasty rings are a fundamental component of mitral repair. They restore the annulus to a normal geometry. Currently, there are dozens of mitral annuloplasty rings approved and available on the market with varying geometries and designs and can be classified into flexible versus rigid. However, two critical needs of MV annuloplasty repair remain unmet. Firstly, restriction of the anteroposterior (AP) dimension is critical to the success of a durable annuloplasty repair by ensuring proper leaflet coaptation and preventing annular dilation[9]. Secondly, the normal human MV annulus has been shown to demonstrate dynamic conformational changes throughout a cardiac cycle, which minimize MV annular and chordal forces[10,11]. Although flexible annuloplasty rings are thought to allow some MV annular motion, they fail to sufficiently restrict the AP distance, which is a common mode of repair failure[12,13]. Conversely, while flat rigid annuloplasty rings can reduce AP dimension and prevent late dilation, these rings significantly restrict the MV annular motion and are associated with increased annular forces[14,15].

Therefore, an optimal mitral annuloplasty ring should demonstrate selective flexibility to allow for the dynamic MV annular dynamic changes throughout the cardiac cycle but at the same time restrict the AP distance to prevent late dilation. We obtained high-resolution cardiac magnetic resonance imaging (MRI) exams from healthy human volunteers. Based on the human imaging results on MV annular dynamics, we designed a selectively flexible mitral annuloplasty ring that simultaneously solves the two main issues by facilitating the native MV annular dynamics while restricting the AP dimension.

This axis-specific mitral annuloplasty ring significantly reduced mitral regurgitation in an ex vivo model and was found to be associated with the lowest secondary chordal forces compared to rigid ring. Mitral annular motion was preserved for up to 6 months in vivo. Mature neoendocardial tissue coverage over the device was found to be complete with full endothelialization in all animals, and no evidence of significant injuries were noted in any downstream, non-targeted tissues.

Methods

Human cardiac MRI acquisition

Healthy human volunteers ($n = 4$) provided informed consent and were imaged using a 3 T MRI scanner (SIGNA Premier, General Electric) and a 60-channel anterior AIR coil coupled with a 30-channel spine coil for cardiac exams. Balanced steady-state free precession (bSSFP) 2D cine cardiac scans were pulse-oximetry gated with breath holds (field of view, 280×280 mm; base matrix, 256×256; spatial resolution, $1.09 \times 1.09 \times 8.00\ mm^3$; 30 phases per cardiac cycle with 10 views per segment; TE/TR, 1.4/3.7 ms; flip angle, 55°). Short axis (SAX) bSSFP cines were acquired for the entire left ventricle and past the mitral annulus for each subject. Ten long axis (LAX) bSSFP cines were acquired to obtain anatomical mitral landmarks based off the 2D SAX cine to include the commissures, trigones, as well as anterior and posterior midpoints with 5 additional LAX bSSFP cines equally spaced in between (Fig. 1a, b). The protocol was approved by the Stanford Institutional Review Board (Protocol #46088).

Mitral annulus tracking and analysis

Mitral annulus tracking was performed using the Cardiac Image Modeling software (CIM v8.0, Tag2D, ©Auckland UniServices Ltd). End-diastolic (ED) and end-systolic (ES) cardiac phases were identified as when the MV closes and aortic valve closes from the LAX images, respectively. Two mitral annular points were identified in each LAX image at ES (Fig. 1c–e). The Cardiac Image Modeling software then automatically tracked the remaining points through all phases of a complete cardiac cycle by finding the optimal nonlinear warp between successive frames on the basis of a pixel sum-of-squared-differences metric[15]. A representative model of the tracked mitral annulus is shown in Fig. 1f. A SAX image at the level of the mitral annulus plane was used to identify mitral annular landmarks closest to the posteromedial commissure (PCOM), anterolateral commissure (ACOM), left trigone, right trigone, anterior midpoint (AM), and posterior midpoint (PM).

The tracked mitral annulus points were then extracted and sorted in a sequential order along the mitral annulus. The annulus motion was isolated by first subtracting the centroid defined by the average of all tracked points, followed by rotating the time-varying annulus points to the least squares plane, calculated via singular value decomposition. The interpolated cubic spline fit was then calculated to generate a smoothed annular geometry. Annular height was estimated by obtaining the sum of the perpendicular distance from the most superior point to the regression plane plus the perpendicular distance from the most inferior point to the regression plane. The intercommissural (IC) distance and AP distance were obtained by calculating the euclidean distance from PCOM to ACOM and AM to PM, respectively, using the interpolated cubic spline fit model. The annular height to intercommissural distance ratio (AHICR) was then calculated by dividing the annular height by IC distance. Lastly, 2D mitral annular area was estimated by calculating the projected mitral annular area onto the regression plane. To compare static annular dimensions, data obtained at midsystole was used. To visualize dynamic data, each measured parameter was temporally resampled using the spline interpolated annulus approximation during the diastolic and systolic intervals to allow comparison of different MRI exams with a range of heart rates. The dynamic measurements were time-shifted such that ED became the first time point. The systole and diastole intervals were then resampled to each occupying half of the cardiac cycle.

Axis-specific mitral annuloplasty ring design

The design goal for the axis-specific mitral annuloplasty ring was to have directional flexibility to best allow for the native mitral annular motion observed in healthy humans. Based on the human imaging data, an ideal mitral annuloplasty ring should be able to transition from a flat profile to a hyperbolic paraboloid shape, known as a saddle shape, while keeping a relatively constant AP annular dimension to prevent dilation. Additionally, the anterior portion of the annuloplasty ring should have sufficient flexibility to accommodate the aortic root and the aorto-mitral dynamics during a normal cardiac cycle. To meet these design criteria, we manufactured our axis-specific annuloplasty ring using a combination of different molded and 3D-printed semi-flexible materials, which in concert with the unique geometry, allowed for simultaneous selective saddle-shape flexibility and AP rigidity. The main body of the ring consisted of a 3D-printed semi-rigid material (FPU 50, Carbon, Redwood City, CA) designed with a flat profile in an incomplete geometry without the anterior portion between the two trigones (Fig. 2a). The unique geometry of the FPU body, specifically the symmetrically oriented kerfed section in the posterior segment allowed for the saddle shape flexibility about the AP axis due to the reduced cross-sectional area and area moment of inertia. By localizing the bending regime of the ring to these kerfed bending zones via geometric manipulation, the ring could maintain relative stiffness in the AP dimension providing structural support and preventing AP dilation. At the trigone positions, two small perforations were made, which were used to tie 3-0 polyester sutures between the two trigones in a continuous fashion. This design decision provides rigidity in tension of the anterior segment, preventing radial expansion or lateral dilation of the ring while allowing for any bending and compression deformation in the anterior segment. The structure was subsequently cast using a mold 3D-printed in UMA90 (Carbon, Redwood City, CA) to adopt a full circular cross-sectional area throughout the ring, filling in the posterior sections and also encasing the anterior polyester suture using an elastic silicone (Shore 20A, P-20, Silicones Inc, High Point, NC) (Fig. 2b). These segments provided additional support, particularly in the kerfed posterior regions, as they dissipate bending energy while buttressing areas of stress concentration. Lastly, to aid the surgical implantation procedure for the ring, the axis-specific mitral annuloplasty ring was wrapped using

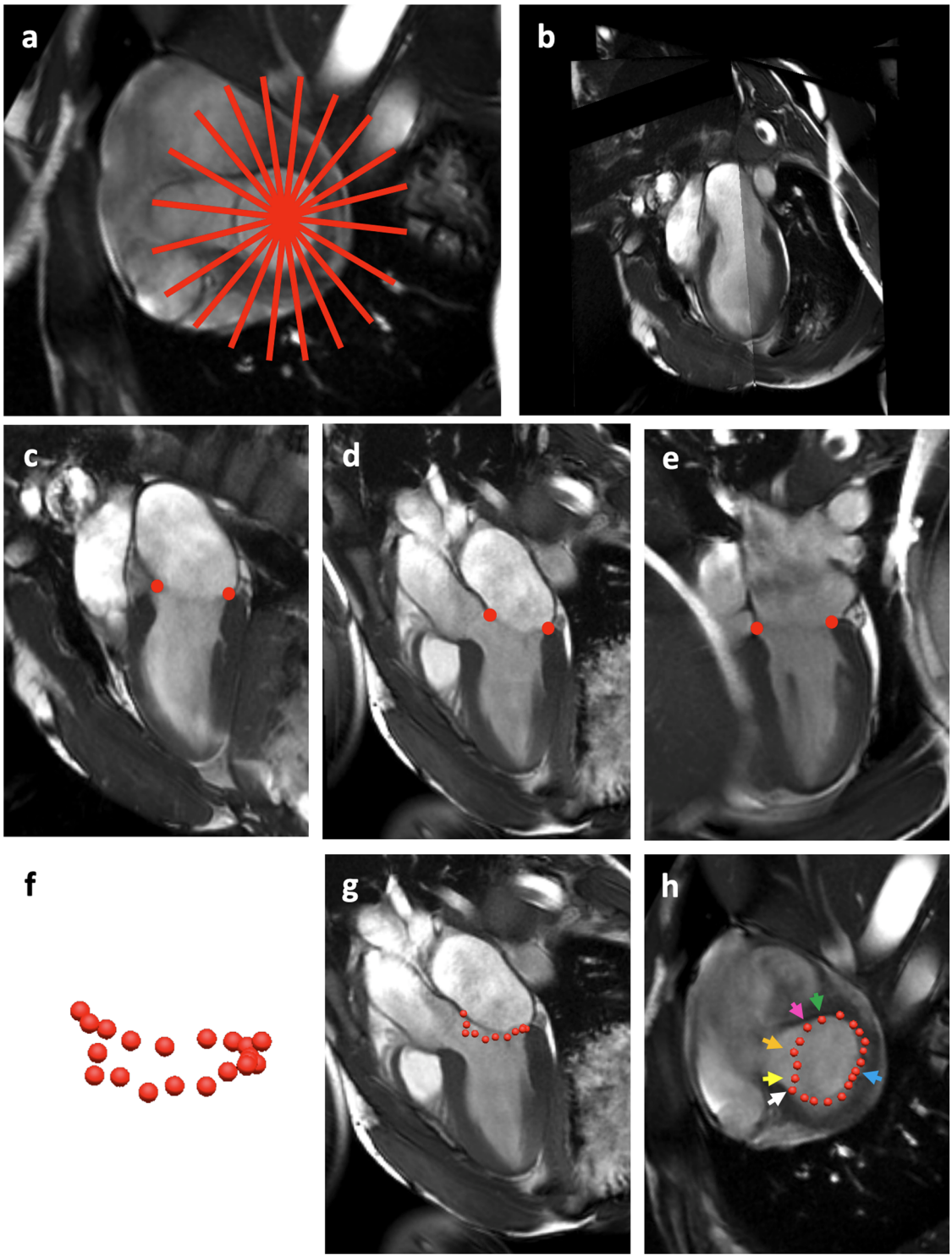

Fig. 1 | Illustration of the long axis cines across the mitral annulus and exemplary tracking features to reconstruct normal human mitral annulus geometry. a Ten long axis cines centered at the mitral valve were acquired to include the commissures, trigones, and anterior and posterior midpoints with 5 additional long axis cines equally spaced in between. **b** Selected long axis slices to demonstrate the 3D reconstructed view. **c**–**e** Demonstration of the two mitral annulus points chosen at end systole for each long axis cine. **f** An exemplary result of the mitral annulus model at end systole reconstructed from the tracking points using the long axis cines. **g** Intersecting of the mitral annulus model with a long axis cine across the anteroposterior midpoints of the mitral annulus. **h** intersecting of the mitral annulus model with a short axis cine closest to the mitral annulus. The colored arrows note the following landmarks: white—posteromedial commissure; yellow—left trigone; orange—anterior midpoint; pink—right trigone; green—anterolateral commissure; blue—posterior midpoint.

polyester fabric with a thin sewing cuff around the outer perimeter of the annuloplasty ring (Fig. 2c). A variety of annuloplasty ring sizes was created to allow for optimal ring sizing for implantation and to allow proper comparisons between the axis-specific ring and commercial rings for all experiments reported in this paper. The exact IC distance and AP distance of each size were designed to be the same as the ones measured from the rigid ring (Carpentier-Edwards Classic, Edwards Lifesciences). The overall geometry and design remained the same across different ring sizes.

Fig. 2 | Design and final prototype of the novel mitral annuloplasty ring. a 3D-printed annuloplasty ring body in a semi-rigid material (FPU 50, Carbon, Redwood City, CA) demonstrating several important features including the kerfed posterior segments to allow lateral bending about the anteroposterior axis, the full thickness segments as well as the width of the posterior segment to provide additional structural support and prevent anteroposterior dilation, incomplete ring design to accommodate the aortic root and the aorto-mitral dynamics, and two small perforations at the trigones to allow the attachment of polyester suture (not shown) for the anterior segment. **b** Complete novel annuloplasty ring design with elastic silicone filling in the posterior segments and encasing the anterior polyester suture using a 3D-printed mold. **c** Final prototype of the novel mitral annuloplasty ring with polyester fabric wrapping the exterior in the flat and saddle geometry. Note a thin strip of sewing cuff at the outer perimeter of the annuloplasty ring for ease of implantation.

Mitral annuloplasty ring mechanical performance characterization

Mechanical testing of the selectively flexible annuloplasty ring (size 32) was performed in two axes and compared to current annuloplasty rings used in clinical practice: a rigid annuloplasty ring (Carpentier-Edwards Classic, Edwards Lifesciences, size 32) and a flexible annuloplasty ring (Annuloflex, LivaNova, size 32). First, to test rigidity in the AP dimension each ring was mounted in a custom 3D-printed mount (UMA90, Carbon, Redwood City, CA) affixed to an Instron 5565 Microtester (Norwood, MA) equipped with a 100 N load cell. The mount was designed to support the ring on the anterior side where the two trigones would be located in vivo, and on the PM point (Supplementary Fig. 1a). The Instron then tensioned each ring in the AP axis at 5 mm/min to a maximum of 10 N. This test was performed five times per ring type. To test each ring's flexibility about the AP axis, the ring was rotated 90 degrees in the Instron and mounted using a separate custom 3D-printed mount (UMA90, Carbon, Redwood City, CA). The new mounting system held the two lateral points of the annuloplasty ring each in a small cylinder, allowing for the ring to bend into the natural saddle shape as the Instron tester placed the ring in compression (Supplementary Fig. 1b). The Instron strain rate was again set to 5 mm/min and the test was performed 5 times per ring type.

Axis-specific mitral annuloplasty ring cytotoxicity testing

To evaluate the cytotoxicity effect of the materials used for the axis-specific annuloplasty ring manufacturing, neonatal rat cardiomyocytes were isolated from 0- to 3-day-old Sprague-Dawley rats of unknown sex using the Pierce™ Primary Cardiomyocyte Isolation Kit (ThermoFisher Scientific, Waltham, MA). The cells were cultured in DMEM, 10% fetal bovine serum, and 1% Penicillin/Streptomycin (Sigma Aldrich, St. Louis, MO) and were pre-plated for 2 hours at 37 °C and 5% CO_2 to remove fibroblasts. The remaining cell suspension was collected and plated in 24-well tissue culture plates at 500,000 cells per well (Corning™ Costar™, Fisher Scientific, Waltham, MA). After 24 hours, the treatment samples (n = 16 per group): 100 µl of PBS and 100 µl of 7.5% sodium hypochlorite were directly added to the cell media as negative and positive controls, whereas FPU and silicon were deposited into transwells suspended over the cardiomyocytes and submerged into the cell media. The FPU and silicon were 3D-printed or cut into a cylinder of 3 mm in diameter and 1 mm in height and were subsequently sterilized using ethylene oxide prior to use. After another 24 hours, the CellTiter-Glo® luminescent cell viability assay (Promega, Madison, WI) was performed. Luminescence was analyzed via microplate reader.

Ex vivo mitral annular dilation system

To evaluate the efficacy of our axis-specific annuloplasty ring hemodynamically and biomechanically, an ex vivo MR model with isolated annular dilation was required. We modified our previously described annular dilation device to mimic annular dilation associated with chronic MR while allowing for ring annuloplasty repair. To achieve these goals, MVs were pre-dilated using a 3D-printed mitral dilator printed in UMA90 (Carbon, Redwood City, CA, Fig. 3a). The dilator was designed with a D-shape of a normal, native mitral annulus to ensure symmetric dilation, and it tapered from a maximal IC distance of 45 mm to 15 mm. The dilated MV was then mounted on a thin, highly elastic MV mount with 1:1 ratio of AP to lateral distance, a dilated mitral annular geometry. This mount was molded from an elastic silicone (Shore 20A, P-20, Silicones Inc, High Point, NC) manufactured using a mold 3D-printed in UMA90 (Carbon, Redwood City, CA). Due to the innate tissue elasticity, the annulus after manual dilation tended not to stay in the maximally dilated state. Therefore, seven additional anchors connected to the custom spring tuning peg system were positioned along the posterior mitral annulus to ensure precise control over annular dilation (Fig. 3b). Each anchor could be independently tightened radially by adjusting the tuning peg to provide just enough tension to hold the annulus in the desired symmetrically dilated geometry. Note that each spring was selected based on the in vivo force measurements of ovine mitral annulus with a spring constant of 2.3 lb/in for the three septal-lateral springs and a spring constant of 2.6 lb/in for the four transverse springs[16]. Using this system, the mitral annulus was effectively fixed in the dilated state. The elasticity of the valve mount allowed for annular dimension reduction from annuloplasty ring repair, but at the same time, the springs mimiced the mitral annular tissue's resistance to dimension reduction.

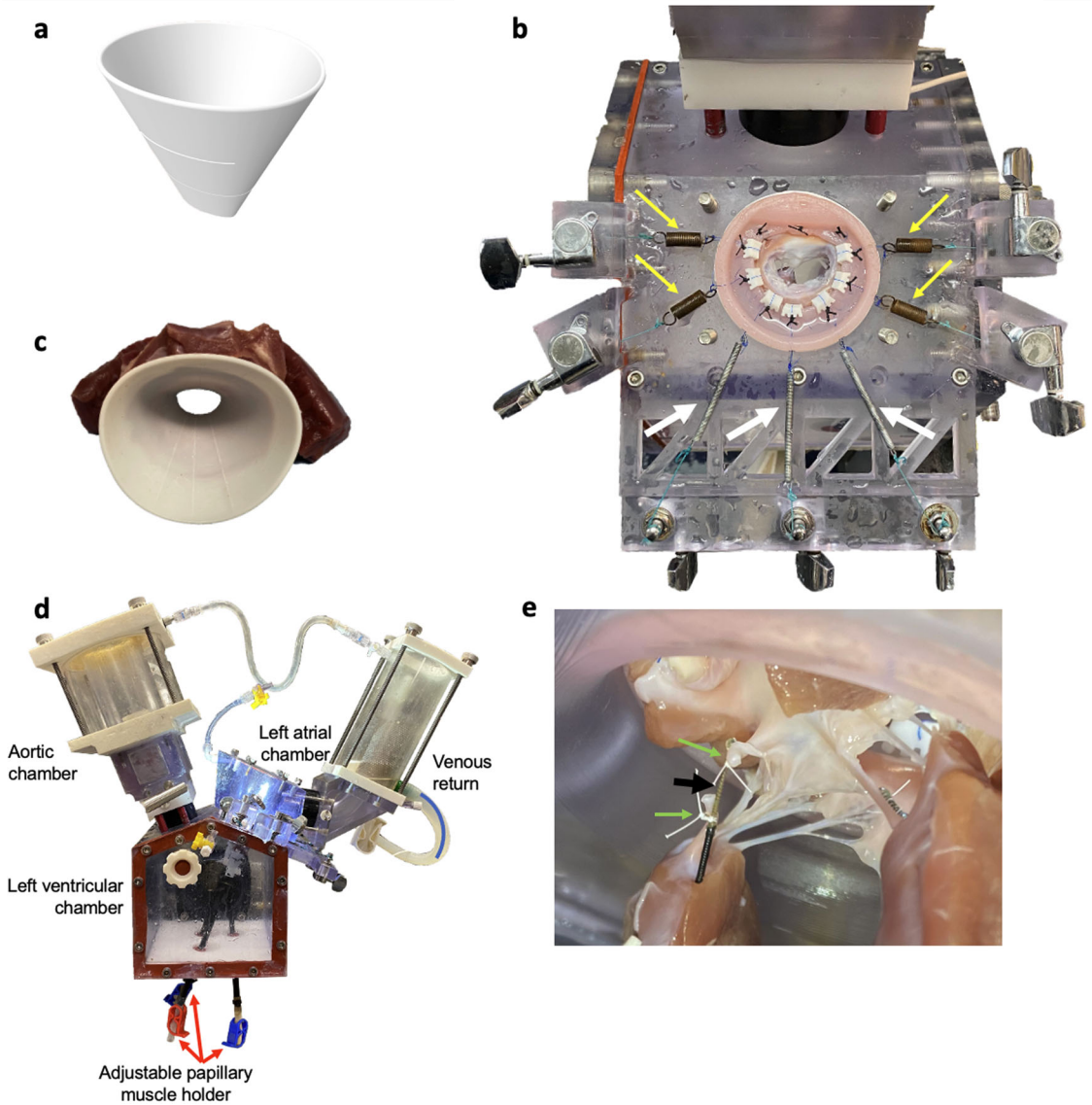

Fig. 3 | Ex vivo mitral annular dilation system and experimental setup. a 3D-printed mitral annular dilator designed with a D-shape of a normal, native mitral annulus for symmetric dilation. **b** The custom left ventricular chamber roof featuring a thin, highly elastic mitral valve mount in a dilated mitral annular geometry and seven anchors connected to the spring tuning peg system (arrows) positioned along the posterior mitral annulus to ensure the mitral valve remains in the dilated geometry while allowing precise control over the degree of annular dilation. The yellow and white arrows annotate springs selected with different spring constants. **c** Illustration of porcine mitral valve dilation by placing the mitral annular dilator across the mitral valve. **d** Labeled photograph of the left heart simulator. **e** High-resolution Fiber Bragg Grating sensors implanted to measure chordal forces. CV-7 polytetrafluoroethylene sutures (green arrows) flanked each side of the strain gauge (black arrow), which were used to attach the sensor to a chord that was then transected after successful sensor attachment.

Ex vivo heart simulation experiment

Fresh porcine hearts were obtained from a local abattoir (Terra Linda Farms, Riverdale, CA), and the MVs were carefully explanted to preserve the leaflets, chordae, papillary muscles, annuli, and surrounding left atrial tissues. MVs with IC distance of 28 mm ($n = 5$) were used to allow sufficient annular dilation to generate MR. The 3D-printed mitral dilator was placed across the explanted MV in the correct dilating orientation, taking care not to injure the chordae tendineae or papillary muscles (Fig. 3c). Once an IC distance of 38 mm was achieved, the dilator was removed from the valve. Interrupted 2-0 silk sutures were used to mount the MV to the elastic silicon mount. These sutures were placed 5 mm away from the annulus in the left atrium cuff to enable maximal annular dilation while allowing sufficient space for ring annuloplasty repair. A continuous 4-0 polypropylene suture along the underside of the valve mount was performed as a hemostatic line to prevent any non-physiologic regurgitation. Lastly, the papillary muscle heads were affixed to the papillary muscle holders using interrupted, pledgeted 2-0 silk sutures, which were then attached to carbon fiber rods within the left ventricular chamber. The custom gasket setup allowed for three degrees of movement for precise papillary muscle positioning and the ability to lock the final position in the same place during the entire experiment.

The ex vivo left heart simulator, which has been previously described[17–21], features a pulsatile linear piston pump (ViVitro Superpump, ViVitro Labs, Victoria, BC, Canada) which generates physiologic hemodynamics in accordance with ISO 5840 in vitro cardiac valve testing standards using the pump controller and software (ViVitest Software, ViVitro Labs, Fig. 3d). An electromagnetic flow probe (Carolina Medical Electronics, East Bend, NC) was used to record the transmitral valvular flow. Ventricular, aortic, and left atrial pressures were measured using pressure transducers (Utah Medical Products, Inc, Midvale, UT). To ensure proper transduction of the flow probe, 0.9% normal saline was used as the test fluid. The linear piston pump was programmed to generate a mean arterial

pressure of 65 mmHg at 70 bpm at the baseline MR state by titrating the compliance chambers and peripheral resistance, which were kept unchanged for the remainder of the experiment. For each test, hemodynamic data was collected and averaged across 10 complete cardiac cycles. Mitral leaflet coaptation heights were measured using a Phillips iE33 system with an S5-1 transthoracic probe (Koninklijke Philips NV, Amsterdam, The Netherlands) and analyzed using the iE33 on-board software and a Siemens Syngo Dynamics workstation (Siemens Medical Solutions USA, Ann Arbor, MI). Chordae tendineae force data were collected by implanting calibrated, high-resolution Fiber Bragg Grating (FBG) sensors (DTG-LBL-1550, 125 μm; FBGS International, Geel, Belgium) as previously described (Fig. 3e)[22]. These sensors were attached to the native chordae using CV-7 polytetrafluoroethylene sutures flanking each side of the strain gauge. The instrumented chordae were then cut between the two suture attachment sites so that force originally on the chordae was imparted to the FBG sensors. Primary and secondary chordae from the anterior and posterior leaflets were measured for each valve. Peak and average chordal forces during systole and the rate of change of force after normalization to mean arterial pressure were analyzed in MATLAB (MathWorks, Natick, MA).

The experimental procedure was designed to analyze the effect of ring annuloplasty repair using different designs on MR and chordal forces. After the baseline MR data were collected, the valve was repaired using our axis-specific annuloplasty ring (size 28), a rigid annuloplasty ring (Annuloflo, LivaNova, size 28), and a flexible annuloplasty ring (Annuloflex, LivaNova, size 28) in a random order. The annuloplasty ring was secured to the annulus using interrupted 2-0 braided polyester sutures. After data collection, the previous annuloplasty ring was removed by cutting the sutures without injuring the annulus. The next annuloplasty ring was implanted in a similar fashion for data collection. During the entire experiment for each valve, the annulus anchors and papillary muscle holders remained in the same position.

In vivo ovine mitral valve operation

For our in vivo studies, only male sheep were used because of the risk of Q fever when working with female sheep. Healthy male Dorset sheep (Joe Pozzi Ranch, CA) weighing ~45 kg were sedated with intramuscular diazepam (0.05–0.2 mg/kg) and induced with intravenous propofol (5–12 mg/kg). Next, the sheep were intubated, and general anesthesia was maintained using 1–3% isoflurane. After undergoing sterile percutaneous placement of a right femoral arterial line, the animals were placed in the left lateral decubitus position and sterilely prepped and draped. For the terminal experiment, the animals were randomized to receive our axis-specific annuloplasty ring (size 28, $n = 6$), rigid annuloplasty ring (Carpentier-Edwards Classic, Edwards Lifesciences, size 28, $n = 6$), or flexible annuloplasty ring (Annuloflex, LivaNova, size 28, $n = 6$). The annuloplasty ring size of 28 was chosen to slightly downsize the mitral annulus to truly reflect the intended annular dimension restriction functionality of annuloplasty rings. For the survival experiment, all animals received our axis-specific annuloplasty ring (size 28). Three sheep survived for 3 months, and 2 sheep survived for 6 months.

A right lateral 4th intercostal space thoracotomy of about 8 cm was performed. The pericardium was incised, and 2-0 silk sutures were used to create a pericardial cradle. Baseline echocardiography was obtained. After the heart was exposed, a heparin bolus of 250 units/kg IV was administered and activated clotting time was measured 5 min later for a target of 480 s prior to initiating bypass. Single-non-pledgeted 2-0 braided polyester purse-string sutures were placed on the proximal aortic arch, as well as superior and inferior vena cava. Direct arterial cannulation was performed using a 16 Fr OptiSite arterial cannula (Edwards Lifesciences, Irvine, CA), inserted into the aorta using the Seldinger technique. Bicaval venous cannulation was then performed using an 18 Fr right-angle cannula (Medtronic, Fridley, MN) inserted into the superior vena cava and a 22 Fr right-angle cannula (Medtronic, Fridley, MN) inserted into the inferior vena cava. A 9 Fr cardioplegia needle (Medtronic, Fridley, MN) was placed into the aortic root. The cardiopulmonary bypass primed with Plasmalyte A was then initiated. After an aortic cross-clamp was applied, 500 mL of cold Del Nido cardioplegia was administered to arrest the heart. The left atrium was opened via the Sondergaard's groove to expose the MV. Non-pledgeted 2-0 braided polyester sutures were placed circumferentially along the mitral annulus. The selected mitral annuloplasty ring was then implanted into the mitral annulus. The left atrium was closed with 4-0 polypropylene sutures in a running fashion. The aortic cross-clamp was then removed, and the cardiopulmonary bypass was weaned off. The aortic, venous, and cardioplegia cannula were removed, and protamine (maximum 2 mg/kg IV) was administered intravenously. Post-repair echocardiogram was repeated. A size 28 chest tube was inserted, secured, attached to a Heimlich valve (Cook Medical, Bloomington, IN), and connected to continuous suction. After satisfactory hemostasis, the incision was closed in layers. For terminal studies, sheep were transported for cardiac MRI after the incisions were closed.

At the conclusion of the experiment, the sheep was euthanized via intravenous potassium chloride. For the survival animals, they were extubated and recovered from anesthesia with inotropic medications weaned. Chest tube was suctioned every 6 h until removed when minimal output was reached. These animals when reaching the terminal endpoint were euthanized via intravenous potassium chloride. The ovine procedures were performed in accordance with the United States National Institutes of Health's "Guide for the Care and Use of Laboratory Animals" (8th Edition, 2011), with approval by the Institutional Animal Care and Use Committee at Stanford University (Protocol #33749).

Ovine cardiac MRI acquisition

The animals were placed in the right lateral decubitus position and secured to the MRI table. Next, the animals were imaged using a 3 T MRI scanner (SIGNA HDxt, General Electric) and an 8-channel cardiac coil for a baseline cardiac exam. bSSFP 2D cine cardiac scans were pulse-oximetry gated with breath holds (field of view, 280×280 mm; base matrix, 256×256; spatial resolution, $1.09 \times 1.09 \times 8.00$ mm^3; 30 phases per cardiac cycle with 6 views per segment; TE/TR, 1.9/4.1 ms; flip angle, 45°; ASSET Phase acceleration, 2). SAX and LAX bSSFP cines were acquired in the same fashion as described above for human subjects. Each terminal ovine subject received baseline cardiac MRI exam up to 5 days prior to MV repair and immediately after the operation. For survival animals, no immediate postoperative cardiac MRI exam was obtained. Additional cardiac MRI exams were performed 1, 3, and 6 months after the operation prior to terminal surgeries.

Ovine brain MRI acquisition

The surviving animals at 3 and 6 months after the operation prior to terminal surgeries underwent brain MRI exam immediately prior to cardiac MRI exam. The animals were placed in the supine position and secured to the MRI table. The animals were imaged using a 3 T MRI scanner (SIGNA HDxt, General Electric) with an 8-channel HRBRAIN coil. Diffusion-weighted, T1-weighted, Fluid-attenuated Inversion Recovery (FLAIR), T2-weighted, T2 star-weighted, and MR angiography images were obtained. Detailed specifications were shared in Supplementary Method 1.

Ovine histopathology and structural analysis

All surviving animals were euthanized at scheduled time points, and limited necropsies were performed, which included examination and collection of the whole heart and brain along with representative sections of the kidneys, lungs, liver, and spleen. Collected tissues were immersion fixed in 10% neutral buffered formalin. Macroscopic observations were noted at necropsy. Tissues with macroscopic changes were collected and findings were recorded on necropsy records. Necropsy records along with the whole heart, brain, and representative samples of the kidneys, lungs, liver, and spleen were provided to StageBio (Mt Jackson, VA) for further assessment.

The whole heart samples were photographed and trimmed to isolate the device from the surrounding tissue. The resultant block of tissue was subjected to Micro Computed Tomography (MicroCT) imaging. The MicroCT images were reviewed for evidence of mineralization, structural disruptions, and mitral annuloplasty ring integrity. The device was

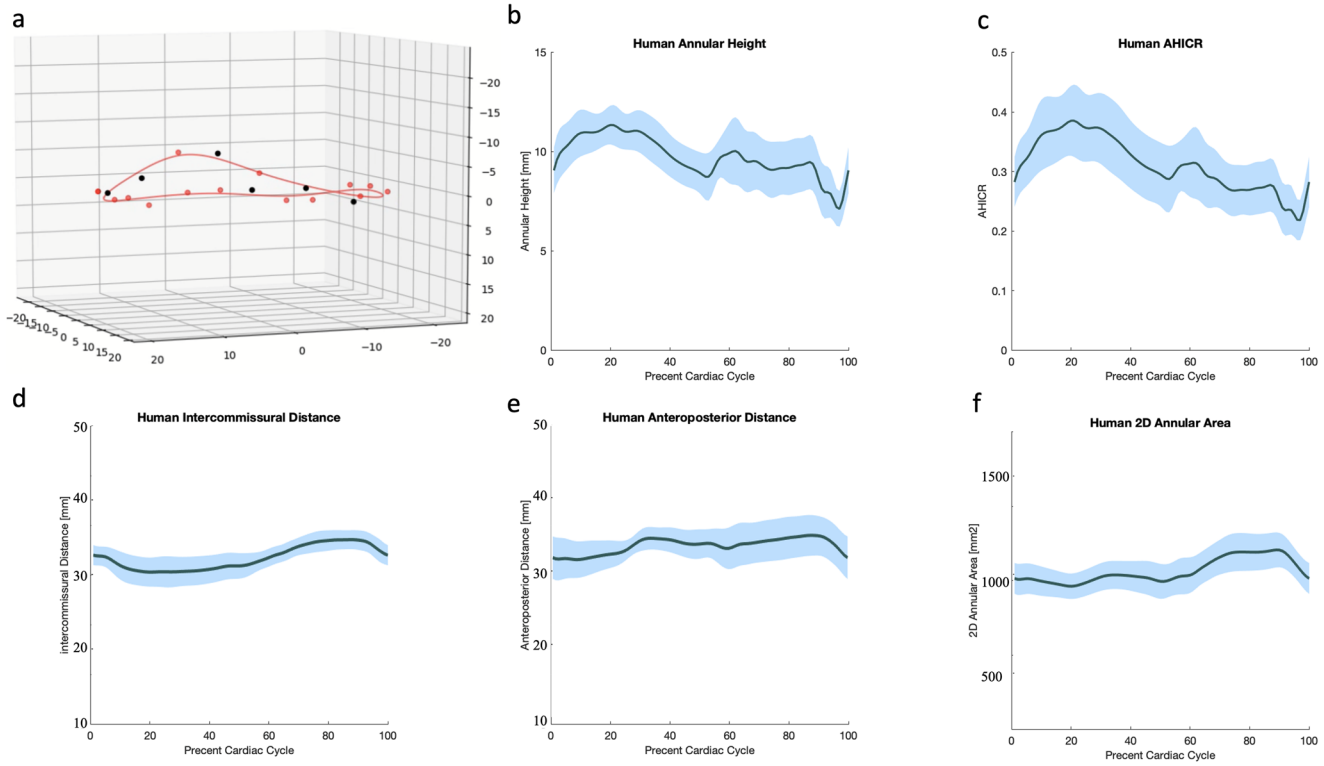

Fig. 4 | Normal human mitral annulus model and dynamic saddle shape geometry changes. a The interpolated cubit spline fit of an exemplary normal human mitral annulus at midsystole. Note the prominent saddle shape. The black markers in a clockwise direction starting in the anterior segment represent the posteromedial commissure, left trigone, anterior midpoint, right trigone, anterolateral commissure, and posterior midpoint. The red markers represent the rest of the tracked annulus points. **b** Mean normal human annular height throughout a cardiac cycle. The annular height increases in systole. **c** Mean normal human annular height to intercommissural distance ratio (AHICR) throughout a cardiac cycle. The AHICR increases throughout systole. **d** Mean normal human intercommissural distance throughout a cardiac cycle. The intercommissural distance remains relatively constant. **e** Mean normal human anteroposterior distance throughout a cardiac cycle. The anteroposterior distance demonstrates a gradual increase. **f** Mean normal human 2D annular area throughout a cardiac cycle. Shaded areas represent standard error. **b**–**f** generated from three human subjects.

processed and embedded in Spurr resin. The medial-lateral and anteroposterior sectioning planes through the tissue and device were captured. One slide was captured from each of the section levels in addition to any trackable gross lesions and stained with Hematoxylin and Eosin (H&E) for assessment of general morphology. Submitted samples of non-cardiac tissues as well as any trackable gross lesions identified at the time of trimming, were trimmed, and embedded in the appropriately sized paraffin block. Each block was sectioned at one level, mounted to slide, and stained with H&E for general morphology. All slides were systematically reviewed and evaluated by a pathologist according to a semi-quantitative scoring system (Supplementary Data 1).

Statistics and reproducibility

For the ex vivo experiment, based on our previous studies, to detect a 15% difference in mean regurgitant fraction with an estimated variance of 16, power of 80%, and confidence interval of 95%, a sample size of 2 is required. To ensure adequate power for the study, a sample size of 5 was chosen. To compare the hemodynamics and biomechanics data measured from the MR baseline and post-repair using the axis-specific, rigid, and flexible annuloplasty rings, repeated measures analysis of variance was performed with post-hoc correction. For the in vivo experiment, based on our previous studies, to detect a 0.3 difference in chordal forces with an estimated variance of 0.02, power of 80%, and a confidence interval of 95%, a sample size of 4 is required. To ensure adequate power for the study, a sample size of 6 was chosen. Variance of each group was assessed using the F test. Paired t-test was performed for static metrics comparison. Continuous variables are reported as mean ± standard deviation unless otherwise specified. Statistical significance was defined at $p < 0.05$ for all tests.

Reporting summary

Further information on research design is available in the Nature Portfolio Reporting Summary linked to this article.

Results

Normal human mitral annulus with dynamic motion

Through high-resolution human cardiac MRI exams and MV annulus tracking (Fig. 1), the normal human MV annulus is shown to exhibit dynamic motion throughout the cardiac cycle (Video 1). The normal human annulus demonstrates increased annular height and AHICR, or accentuated saddle shape, throughout systole with relatively constant IC distance (Fig. 4). Additionally, the AP distance shows a gradual increase in distance. At midsystole, the annular height is estimated to be 11.4 ± 1.6 mm with an average AHICR of 0.4 ± 0.1 mm (Supplementary Data 2).

Axis-specific mitral annuloplasty ring with selective flexibility

Based on the human imaging data, a selectively flexible mitral annuloplasty ring is designed and manufactured with axis-specific flexibility to facilitate the native MV annular dynamics while restricting the AP dimension (Fig. 2).

Rather than examining the fundamental material properties of the rings, we sought to examine how each ring would function in an in vivo setting in response to forces and geometric constraints. Under the AP tensile force application, the axis-specific annuloplasty ring performs similarly, albeit slightly less rigid, compared to the rigid annuloplasty ring, and behaves differently from the flexible annuloplasty ring, which exhibits wider AP separation under the same load (Supplementary Fig. 2a). At 1 N of tensile force the axis-specific ring experiences 0.31 ± 0.02 mm of anterior-

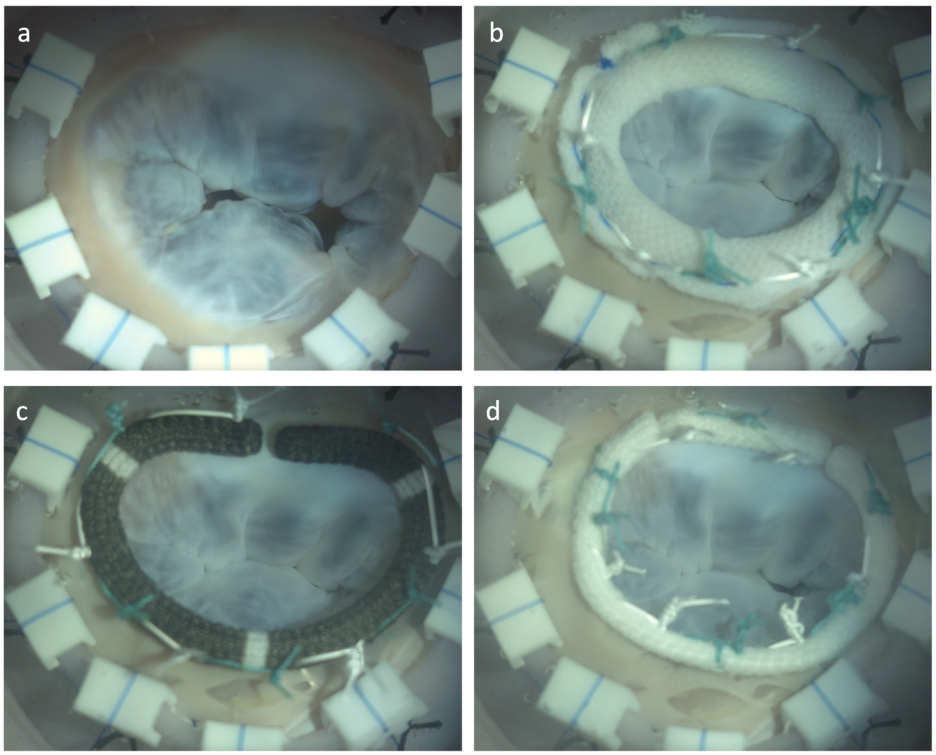

Fig. 5 | En face views of a representative porcine mitral valve in the ex vivo experiment. a The porcine mitral valve in systole mounted to the mitral annular dilation system. Note the lack of proper leaflet coaptation and regurgitant areas. **b** The same porcine mitral valve in systole after repair using the novel mitral annuloplasty ring. Note the restoration of leaflet coaptation. **c** The same porcine mitral valve in systole after repair using a rigid mitral annuloplasty ring. Note adequate leaflet coaptation. **d** The same porcine mitral valve in systole after repair using a flexible mitral annuloplasty ring. Note a small regurgitant area and less leaflet coaptation compared to (**b**, **c**). The flexible ring also lost the "D" shape of a native, normal mitral annular geometry.

posterior extension. At the same force, the rigid annuloplasty ring experiences 0.34 ± 0.14 mm of anterior-posterior extension and the flexible ring experiences 3.91 ± 0.28 mm of extension. On the other hand, under the compressive force in the lateral direction, the axis-specific annuloplasty ring demonstrates similar behavior to the flexible ring, with both flexing and requiring less compressive force to achieve the same displacement compared to the rigid ring (Supplementary Fig. 2b). The axis-specific ring reaches 1.5 mm of displacement at 0.40 ± 0.08 N of compressive force. To reach the same displacement, the rigid annuloplasty ring requires 3.94 ± 1.15 N of force and the flexible ring requires 0.06 ± 0.004 N. Note that load versus extension is used rather than the more traditional stress versus strain to more accurately compare the three rings' functional characteristics.

Axis-specific annuloplasty ring materials with low cytotoxicity

The cytotoxicity results of the materials used to manufacture the axis-specific annuloplasty ring are shown in Supplementary Fig. 3. Compared to PBS, FPU 50 (Carbon, Redwood City, CA) and silicone treatments are not associated with a decrease in cardiomyocyte viability (FPU vs PBS: 9118.6 ± 2824.7 relative light unit (RLU) vs 9751.3 ± 1222.9 RLU, $p = 0.42$; silicone vs PBS: 9376.3 ± 1550.0 RLU vs 9751.3 ± 1222.9 RLU, $p = 0.45$). As a positive control, sodium hypochlorite is associated with significantly decreased cardiomyocyte viability compared to PBS (79.9 ± 32.4 RLU vs 9751.3 ± 1222.9 RLU, $p = 0.0001$).

Ex vivo hemodynamics and biomechanics performance

The ex vivo mitral annular dilation system (Fig. 3) successfully generates MR in all porcine MV samples (Fig. 5a) with an effective regurgitation fraction (RF) of 30.0 ± 5.8% and leaflet coaptation height of 0.5 ± 0.1 cm. Ring annuloplasty repair using the axis-specific, rigid, and flexible ring effectively restored MV competency and reduced RF to 4.7 ± 2.7% ($p = 0.001$), 2.4 ± 3.2% ($p = 0.001$), and 17.8 ± 10.0% ($p = 0.004$), respectively. The leakage rate also reduces from 61.3 ± 24.9 mL/s at dilated baseline to 2.5 ± 5.7 mL/s using the axis-specific ring ($p = 0.004$), 0.7 ± 6.7 ml/s using the rigid ring ($p = 0.004$), and 25.8 ± 18.9 ml/s using the flexible ring ($p = 0.003$). The en face views of an example of a porcine MV demonstrate that leaflet coaptation is improved to a varied degree following ring annuloplasty repair (Fig. 5b–d). Note that a small regurgitant area is still present following flexible ring annuloplasty repair, likely due to a loss of the mitral annular "D" shape of the flexible ring, whereas repairs using the axis-specific and rigid rings demonstrate adequate MV coaptation. The leaflet coaptation heights following repair using the axis-specific, rigid, and flexible ring, compared to dilated baseline, improve to 1.2 ± 0.2 cm ($p = 0.01$), 1.1 ± 0.2 cm ($p = 0.01$), and 0.7 ± 0.1 cm ($p = 0.01$), respectively. Furthermore, flexible ring annuloplasty repair is associated with significantly decreased leaflet coaptation height compared to that after repairs using the axis-specific ring ($p = 0.004$) and the rigid ring ($p = 0.01$).

A summary of hemodynamic data is shown in Supplementary Table 1. The mean transmitral flow and left heart pressure tracings across all five samples also confirmed the generation of significant MR in the dilated state, as evidenced by flow reversal during systole and the lower arterial and left ventricular pressures (Fig. 6a, b). Ring annuloplasty repair using the flexible ring demonstrates some elimination of MR compared to the dilated baseline, noting the residual flow reversal during systole (Fig. 6a). Compared to RFs achieved using the axis-specific and rigid rings, RF after flexible ring annuloplasty repair is significantly higher ($p = 0.04$ and $p = 0.04$, respectively). Similarly, compared to the leakage rates measured using the axis-specific and rigid rings, leakage rate after flexible ring annuloplasty repair is significantly higher ($p = 0.04$ and $p = 0.03$, respectively). Ring annuloplasty repair successfully restores the mean aortic pressure and left ventricular pressure from 64.6 ± 0.7 mmHg and 32.3 ± 0.9 mmHg at dilated baseline to 86.0 ± 5.8 mmHg and 39.3 ± 2.9 mmHg using the axis-specific ring ($p = 0.001$ and $p = 0.01$), 87.8 ± 6.8 mmHg and 40.8 ± 2.8 mmHg using the rigid ring ($p = 0.001$ and $p = 0.002$), and 82.3 ± 6.7 mmHg and 39.1 ± 2.4 mmHg using the flexible ring ($p = 0.003$ and $p = 0.004$), respectively (Fig. 6b). Otherwise, the mean arterial and left ventricular pressure tracings are similar after repair using the axis-specific, rigid, and flexible rings.

By restoring leaflet coaptation and MV competency, ring annuloplasty resulted in significantly lowered forces in the primary chordae (Supplementary Table 2, Fig. 6c). Specifically, the peak force, average force, and rate of change of force decrease from 0.6 ± 0.2 N, 0.4 ± 0.2 N, and 6.3 ± 2.1 N/s at dilated baseline to 0.4 ± 0.1 N ($p = 0.0004$), 0.3 ± 0.1 N ($p = 0.01$), and

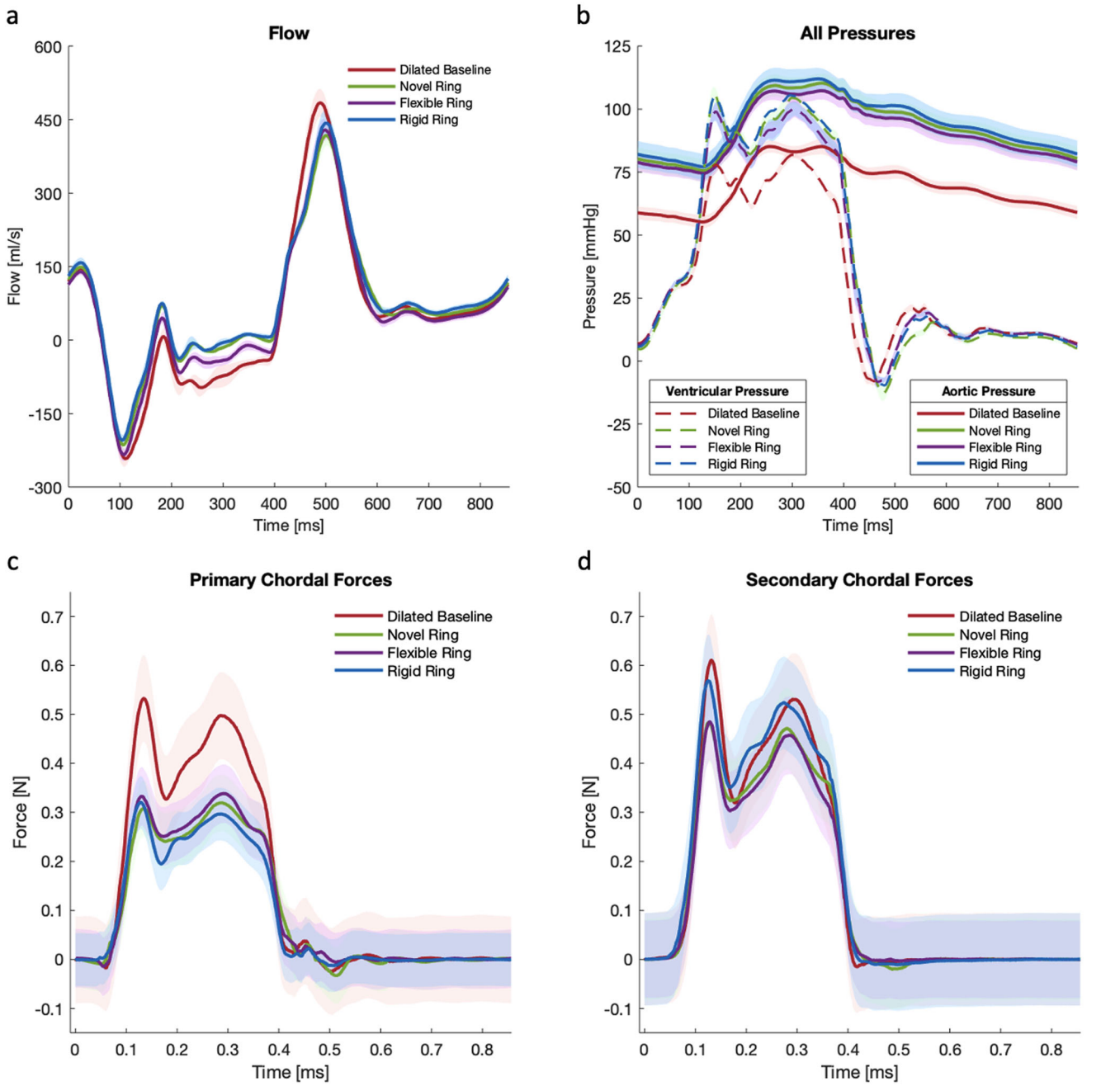

Fig. 6 | Flow and pressure tracings as well as chordal force profiles ($n = 5$). a Mean transmitral flow tracings confirmed mitral regurgitation at dilated baseline, as well as reduced regurgitation after ring annuloplasty repair. Note the residual mitral regurgitation after repair using a flexible annuloplasty ring, as evidenced by the flow reversal during systole. **b** Ring annuloplasty repair restored the mean aortic and left ventricular pressures. **c** Primary chordal forces significantly decreased after ring annuloplasty repair. **d** Secondary chordal forces decreased after ring annuloplasty repair with the axis-specific mitral annuloplasty ring being associated with a favorable secondary chordal force profile compared to that of the rigid ring. Shaded regions represent standard error.

4.0 ± 2.0 N/s ($p = 0.001$) using the axis-specific ring; 0.3 ± 0.1 N ($p = 0.001$), 0.2 ± 0.1 N ($p = 0.01$), and 4.1 ± 1.6 N/s ($p = 0.01$) using the rigid ring; and 0.4 ± 0.1 N ($p = 0.002$), 0.3 ± 0.1 N ($p = 0.02$), and 4.0 ± 1.6 N/s ($p = 0.001$) using the flexible ring, respectively. There is no difference in peak force, average force, or rate of change of force measured in primary chordae after using different annuloplasty rings ($p = 0.22$, $p = 0.34$, and $p = 0.99$, respectively). Ring annuloplasty repair also decreases chordal forces in the secondary chordae, but the difference is not statistically significant (Supplementary Table 2, Fig. 6d). However, the use of an axis-specific ring compared to the rigid ring is associated with significantly lower peak force (0.5 ± 0.3 N vs 0.6 ± 0.3 N, $p = 0.03$), average force (0.3 ± 0.2 N vs 0.4 ± 0.2 N, $p = 0.05$), and rate of change of force (3.5 ± 1.9 N/s vs 5.3 ± 2.0 N/s, $p = 0.01$) in secondary chordae. No difference is observed in the secondary chordal forces using different annuloplasty rings.

Large animal mitral annulus motion immediately after axis-specific ring repair

All ovine subjects show competent MV without MR at baseline and immediately after ring annuloplasty repair regardless of the ring received. The ejection fraction at preoperative baseline vs after axis-specific ring repair is 51.3 ± 1.7% vs 50.2 ± 9.3% ($p = 0.77$), at preoperative baseline vs after rigid ring repair is 52.0 ± 2.1% vs 50.9 ± 8.2% ($p = 0.72$), and at preoperative baseline vs after flexible ring repair is 50.8 ± 3.0% vs 49.8 ± 9.3% ($p = 0.84$). After axis-specific ring annuloplasty repair (Supplementary Fig. 4)

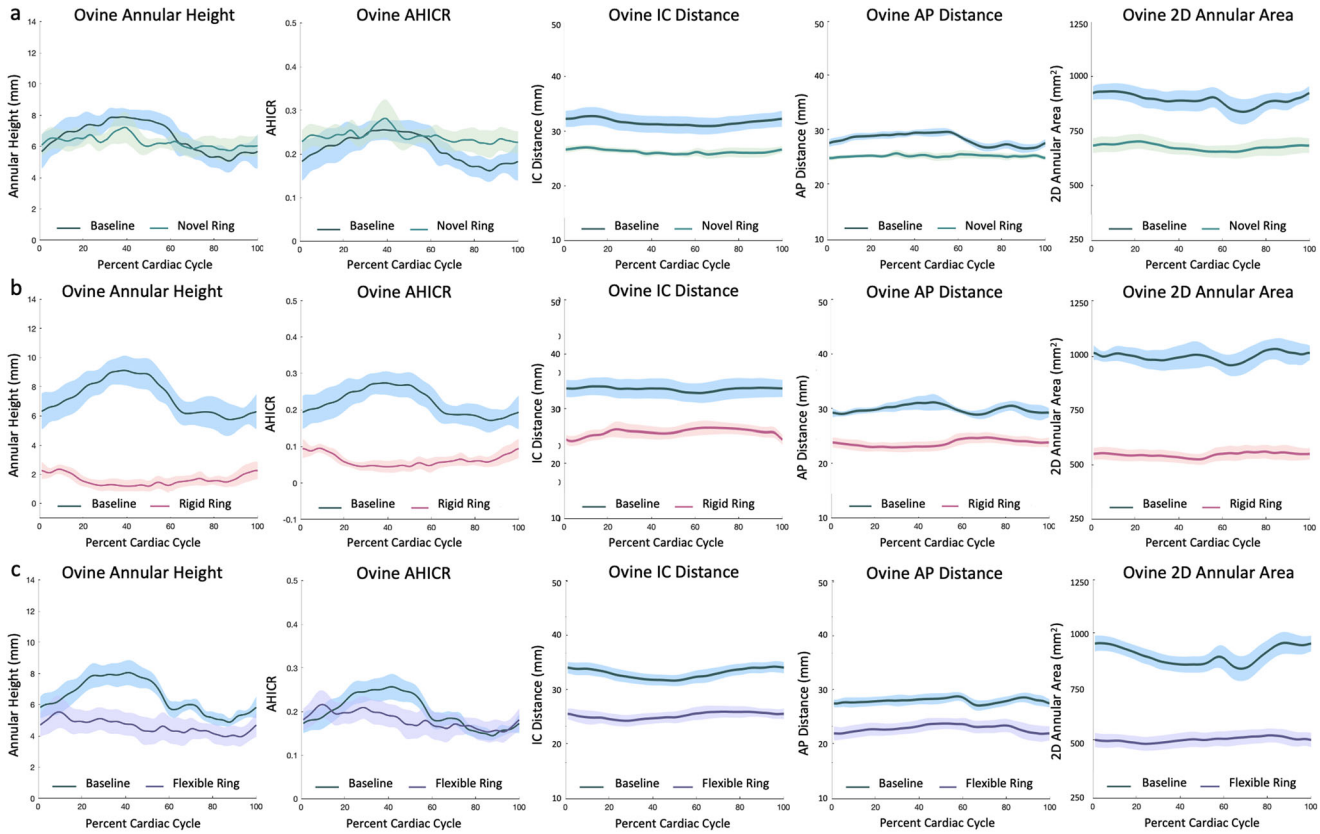

Fig. 7 | Mean ovine mitral annular dynamics at preoperative baseline and after ring annuloplasty repair using the novel, rigid, or flexible ring ($n = 6$). a Mean ovine annular dynamics at preoperative baseline and after novel ring repair. **b** Mean ovine annular dynamics at preoperative baseline and after rigid ring repair. **c** Mean ovine annular dynamics at preoperative baseline and after flexible ring repair. Novel ring demonstrates similar annular height and annular height to intercommissural distance ratio (AHICR) compared to preoperative baseline, suggesting the saddle shape geometry of the novel ring. These two metrics also show similar trends in variation compared to preoperative baseline throughout a cardiac cycle, suggesting the geometry changes over time. The flexible ring demonstrates a slightly decreased annular height and AHICR, thus a slightly lessened saddle shape geometry compared to preoperative baseline, but with dynamic geometric changes over time. The rigid ring demonstrates primarily a flat geometry, illustrated by the decrease in annular height and AHICR compared to preoperative baseline. This geometry remains relatively stable throughout a cardiac cycle. Intercommissural distance, anteroposterior distance, and 2D annular area decrease after ring annuloplasty repair compared to preoperative baseline. Shaded areas represent standard error. Blue—preoperative baseline; green—novel ring repair; red—rigid ring repair; purple – flexible ring repair.

compared to preoperative baseline, there is no difference in midsystolic annular height, midsystolic AHICR, or AHICR variance (Supplementary Data 2, 4–6). Compared to the ovine annular geometry at preoperative baseline (Video 2), the MV annulus after axis-specific ring repair (Video 3) demonstrates a similar saddle shape geometry at midsystole (Supplementary Fig. 5). The annular height and AHICR show similar dynamic changes throughout a cardiac cycle between the preoperative baseline and after axis-specific ring repair (Fig. 7a). The midsystolic IC distance, midsystolic AP distance, variance of AP distance, and midsystolic 2D annular area are all decreased after axis-specific ring repair compared to preoperative baseline (Supplementary Data 2, 4–6, Fig. 7a).

After rigid ring annuloplasty repair (Video 4) compared to preoperative baseline, midsystolic annular height, midsystolic AHICR, and AHICR variance are significantly reduced (Supplementary Data 2, 4–6, Fig. 7b, Supplementary Fig. 5). The MV annulus after rigid ring repair demonstrates a fixed, flat geometry at midsystole, distinctly different from the ovine annular geometry at preoperative baseline. The annular height and AHICR are markedly reduced without dynamic changes throughout a cardiac cycle after rigid ring repair compared to the preoperative baseline (Fig. 7b). The midsystolic IC distance, midsystolic AP distance, variance of AP distance, and midsystolic 2D annular area are all decreased after rigid ring repair compared to preoperative baseline (Supplementary Data 2, 4–6). In comparison, after flexible ring annuloplasty repair (Video 5) compared to preoperative baseline, there is no difference in midsystolic annular height, midsystolic AHICR, or AHICR variance (Supplementary Data 2, 4–6). The MV annulus after flexible ring repair demonstrates a similar saddle shape geometry at midsystole (Supplementary Fig. 5). The annular height and AHICR after flexible ring repair show time-varying changes, although lessened compared to preoperative baseline throughout a cardiac cycle (Fig. 7c). The midsystolic IC distance, midsystolic AP distance, and midsystolic 2D annular area are decreased after flexible ring repair compared to preoperative baseline, but the variance of AP distance remains similar (Supplementary Data 2, 4–6).

Large animal mitral annulus motion months after axis-specific ring repair

All survival ovine subjects show competent MV without MR before surgery as well as 3 and 6 months after axis-specific ring annuloplasty repair. The ejection fraction at preoperative baseline vs 3 months after axis-specific ring repair is 49.6 ± 4.7% vs 46.2 ± 3.4% ($p = 0.06$). Six months after axis-specific ring annuloplasty repair is found to have an average ejection fraction of 53.8 ± 4.2%, similar to that measured at baseline (54.0 ± 3.7%, $p = 0.61$). Video 6 shows that the MV annulus, even at 6 months after axis-specific ring annuloplasty repair, continues to have dynamic changes throughout a cardiac cycle while demonstrating a saddle shape geometry at midsystole. Midsystolic annular height is similar between preoperative baseline and 1, 3, and 6 months after axis-specific ring annuloplasty repair (Supplementary Table 3). Additionally, midsystolic AHICR and AHICR variance are also found to be similar between preoperative baseline and 1, 3, and 6 months after axis-specific ring annuloplasty repair (Supplementary Table 3). The

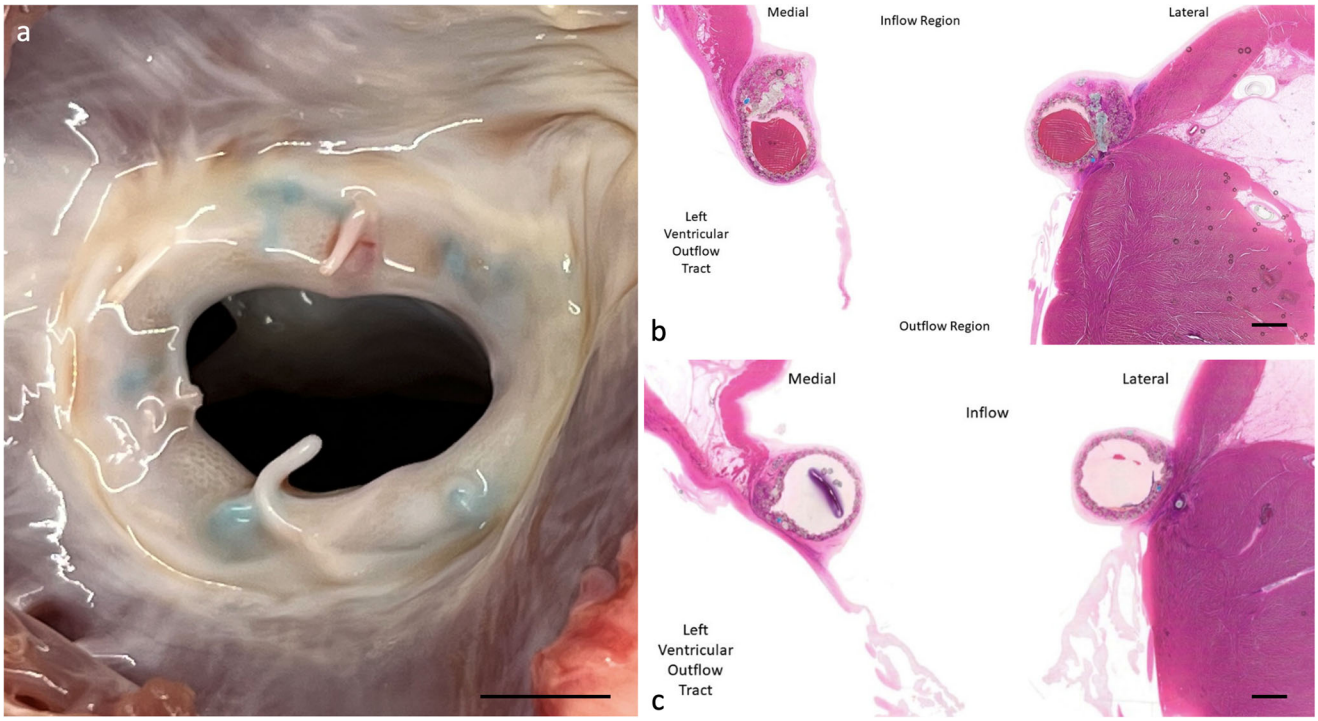

Fig. 8 | Exemplary gross pathology image and Hematoxylin and Eosin images of the mitral valves at 3 and 6 months after novel ring implantation. a Gross images revealed appropriate integration of the axis-specific ring within the native annulus characterized by complete device coverage by mature, endothelialized neoendocardium. Scale bar = 1 cm. At 3 (**b**) and 6 (**c**) months after ring implantation, the axis-specific rings were attached to the left atrium by neoendocardium. The aorto-mitral curtains and anterior mitral leaflets were connected to the undersurface of the axis-specific rings. At the lateral aspect, the native posterior mitral valve leaflets extended from the inferior edges of the novel rings at the left ventricular surface. Scale bars = 2 mm.

midsystolic IC distance, midsystolic AP distance, variance of AP distance, and midsystolic 2D annular area are all decreased at 1, 3, and 6 after axis-specific ring repair compared to preoperative baseline (Supplementary Table 3).

Large animal long-term structural integrity of the axis-specific ring in vivo

At 3 and 6 months after axis-specific ring implantation, none of the annuloplasty rings demonstrates detectable changes or major fragmentation by MicroCT. The rings maintain oval contours without major disruptions or conformational changes observed grossly or via MicroCT examination. Small, focal opacities consistent with mineralization are observed in three of the five animals (Supplementary Fig. 6). These opacities appear outside of axis-specific ring and within the endothelialization tissue covering the ring.

Large animal long-term safety and biocompatibility after axis-specific ring implantation

There are no unscheduled mortalities among the surviving animals. At both 3 and 6 months after axis-specific ring implantation, no overt injury to the native MV leaflets, restriction in leaflet movement at the leaflet base, or adverse findings that may affect coaptation are noted grossly. On further histology assessment, mature neoendocardial tissue coverage over the device is found to be complete with full endothelialization in all animals (Fig. 8). Overall device-related inflammation comprises mild, foreign body infiltrate (Supplementary Data 1, Supplementary Table 4). One animal survived 6 months demonstrates a visible nodule on the inflow surface that is microscopically consistent with an area of osseous metaplasia. No evidence of infective endocarditis is found.

In all downstream, non-targeted tissues, no thrombus or notable significant findings are identified except for bilaterally light redness of renal crests in all animals (Supplementary Fig. 7). Brain MRI does not show any abnormally high signal lesions to suggest any ischemic lesions or cerebral infarction. No apparent safety concerns of intolerance associated with the axis-specific ring are noted. Additional gross pathology photographs are listed in Supplementary Figs. 8–11.

Discussion

We design and manufacture a axis-specific selectively flexible mitral annuloplasty ring based on high-resolution human MRI imaging data. Through a series of comprehensive experiments from bench to pre-clinical large animal models, this axis-specific ring demonstrates selective flexibility to facilitate the native mitral annular dynamics during a complete cycle while restricting the AP annular dimension to prevent dilation, effectively solving the two main critical challenges that current mitral annuloplasty rings face. This unique mitral annuloplasty ring not only demonstrates excellent capacity in eliminating MR with low chordal forces ex vivo, but also successfully allows for the native mitral annular dynamic motion in vivo.

The effect of preserving the saddle shape of the mitral annulus after ring annuloplasty repair has been investigated. Rigid saddle-shaped annuloplasty rings have been shown to be associated with improved leaflet coaptation[23,24], reduced mechanical strain on the leaflets[25], chordae[26], and the annulus[14], as well as increased leaflet curvature[27,28] using numerical simulations, ex vivo simulations, in vivo large animal models, and clinical results from patients who underwent ring annuloplasty repair. It appears well-supported that the saddle shape of the mitral annulus plays a significant role in the function of MV apparatus with mechanical advantages. Conversely, flexible mitral annuloplasty rings have been shown to allow some MV annular area changes[29] and were associated with reduced anterior mitral leaflet strain[15]. Additionally, patients who received flexible rings demonstrated improved left ventricular shortening, lower peak velocity, and improved left ventricular systolic function compared to those who received rigid rings[29,30]. These results suggest that flexible rings interfere less with the normal movements of the MV annulus during the cardiac cycle, and that they may perform better than rigid rings in patients with MR due to degenerative disease[29]. Therefore, we hypothesized that an optimal mitral

annuloplasty ring should allow the normal mitral annular dynamics and facilitate the saddle shape geometry transition during a cardiac cycle.

As was visualized through our high-resolution cardiac MRI exams obtained in this study, the normal human mitral annulus transitions into a profound saddle shape during systole, consistent with the findings from prior studies[10,11]. In addition to annular height, the AHICR is another metric used in quantifying the "saddle-shape-ness" of the mitral annulus, which has been found to be conserved across species[11,31]. This metric is also used in designing and prototyping our axis-specific mitral annuloplasty ring. To achieve the ideal design of an axis-specific mitral annuloplasty ring that can transition between a saddle and a flat shape, we use a semi-rigid material for the main body of the ring. The selective flexibility to allow the ring to bend about the AP axis was achieved through the precise geometry tuned via the thickness and shape of the bending segments in the posterior portion of the ring. The geometry and material stiffness of the non-kerfed segments provided sufficient structural rigidity to effectively prevent AP dilation. Although one could also use flexible material for the anterior and posterior portions of the ring to allow for a transition between a saddle and flat geometry, this type of design has a significant flaw of not being able to restrict the AP dimension. It has been hypothesized that AP distance is an important variable that can affect the long-term repair durability after ring annuloplasty repair. Although quite a few studies demonstrated the advantages of using flexible over rigid annuloplasty rings in clinical practice, recent studies, including randomized control trials failed to show clinical outcome differences between flexible and rigid annuloplasty rings[13,30]. One important observation is that patients with ischemic MR who received flexible ring annuloplasty repair demonstrate higher incidences of residual MR of moderate degree or greater compared to those who received rigid rings[12]. In fact, it has been shown that the MV annular dynamics and dimensions are affected by various MV pathologies, commonly demonstrating increased MV area and AP distance[11,32,33]. Therefore, the lack of AP dimension fixation in flexible rings may be a key contributor in the high recurrence of MR after repair.

In this study, we design, manufacture, and evaluate the performance of this axis-specific mitral annuloplasty ring in a comprehensive manner, encompassing ex vivo hemodynamics and biomechanics evaluation, as well as in vivo MV annular dynamics analysis in a pre-clinical large animal model. In the ex vivo experiment, a precisely controlled MV annular dilation system is designed to effectively compare the performance among mitral annuloplasty rings of different flexibility. Other previously established ex vivo MR models[17,34] are not used in this study because additional confounding factors from other repair techniques used to repair MR would be introduced whereas the isolated effect of annular size reduction from different annuloplasty rings is one of the primary outcomes of this experiment. While the rigid, flexible, and axis-specific rings all result in a significant reduction in MR, the flexible annuloplasty ring performs least effectively among all. Our ex vivo dilation system effectively mimics the MR diseased state with annular dilation with appropriate resistance to annular reduction. It is not surprising that flexible rings with significant laxity in their 3D geometry perform the worst in re-establishing adequate leaflet coaptation and therefore resulting in higher post-repair MR. This axis-specific ring demonstrates similar excellent effectiveness in eliminating MR compared to a rigid ring, suggesting the important role in its design to maintain a relatively constant AP dimension.

In the ex vivo experiment, all annuloplasty rings successfully reduce primary chordal forces regardless of the ring flexibility. This finding is consistent with our previous studies which show that after MV competency is restored, primary chordae forces would decrease[17,18,34–36]. As the primary chordae tendineae resume their principal role in ensuring proper leaflet coaptation, the secondary chordae support the majority of forces during systole. Though the secondary chordal forces do not change drastically overall after ring annuloplasty repair, the axis-specific ring demonstrates a significant reduction in secondary chordal forces compared to the rigid ring. Ring flexibility has been shown to reduce posterior suture forces[37], which may in turn affect chordal forces. Thus, the flexibility about the AP axis that allows for a saddle-shape geometry is likely one of the key factors that provide additional mechanical advantages over a flat rigid ring[14,25].

In addition to the axis-specific ring's capacity to effectively reduce MR while maintaining a low chordal force profile, the in vivo pre-clinical large animal experiment confirms our axis-specific ring's ability to facilitate MV annular dynamics. Annular height and AHICR are two important metrics that indicate the saddle-shape geometry of the MV annulus. It is remarkable that the axis-specific ring not only demonstrates similar static annular height and AHICR values compared to those measured from preoperative baseline, but these two metrics also demonstrate similar time-varying dynamics throughout a cardiac cycle compared to those from preoperative baseline. Even at 1-, 3-, and 6-month post ring implantation, the static annular height and AHICR as well as AHICR variance remain statistically similar to those obtained at baseline. These critical findings suggest that this axis-specific ring not only preserves the saddle shape geometry of the MV annulus, but also allows for annular dynamic changes between a saddle shape and a more planar geometry. In contrast, rigid ring repair demonstrates significantly reduced annular height and AHICR, and these two metrics remain relatively constant throughout a cardiac cycle, suggesting a fixed, flat MV annular geometry. These findings not only validate the MV annulus tracking and analysis methodology, but also confirm the success of the axis-specific ring design in achieving selective flexibility that allows for the saddle shape geometry transition. Interestingly, the flexible ring although demonstrates dynamic MV annular geometry throughout a cardiac cycle, the degree of changes in annular height and AHICR are dampened. These results suggest that flexible rings, while they can allow some MV annular geometric changes, have limited capability in supporting MV annular dynamics. In comparison, the axis-specific ring's meticulous design maximizes its ability to allow for natural MV annular dynamics for at least 6 months after ring implantation in a large animal model.

Furthermore, the in vivo results validate the ability of the axis-specific ring to prevent AP dilation, similar to what we observed after rigid ring repair. The AP distance and variance restriction features of the axis-specific ring remain evident up to 6 months after ring implantation. However, the flexible ring fails to demonstrate decreased AP dimension variance compared to preoperative baseline, reflecting its major weakness in AP dilation prevention. Note that the midsystole AP distance, IC distance, and 2D annular area are reduced after ring annuloplasty repair in vivo regardless of the ring type. Specifically, the axis-specific ring continues to provide intentional structural restriction to maintain reduced misystolic IC distance and 2D annular area for up to 6 months following ring implantation. In this experiment, undersized rings are used in vivo to simulate the effect of annular size reduction in clinical practice for patients with MR. As the rigid ring has no flexibility, the projected planar or 2D annular area is restricted significantly. The flexible ring, because it is flexible in all axes throughout the ring, would accommodate an increase in annular height during midsystole by reducing 2D annular area, therefore also resulting in significant planar area reduction. Additionally, AP dimension reduction is an important annuloplasty ring design feature to prevent future annular dilation that may lead to MR recurrence and adverse left ventricular remodeling.

The other important objective of performing survival large animal experiments is to complete histopathological and device structural evaluation. Overall appropriate integration of the device within the native mitral annulus is observed in all animals with mature, complete endothelialization. Mineralization and osseous metaplasia are also observed but it is known that ovine models commonly demonstrate osseous metaplasia as part of the positive healing response. Overall, device-related inflammation is considered well within what is expected for intracardiac devices. This is indicative of excellent biocompatibility. Additionally, no downstream effects are present suggesting no apparent safety concerns or intolerance associated with the axis-specific annuloplasty ring. One interesting finding from gross pathology evaluation is bilaterally light redness of renal crests observed in all animals. All animals received aspirin therapy for the entire postoperative duration as per guideline recommendations for human patients[38]. It is known that nonsteroidal anti-inflammatory drugs, especially when overdosed or used for prolonged period of time, can cause renal toxicity and acute kidney injury, and this effect is especially prominent in canines[39]. Though studies on the effect of NSAIDs on

ovine kidney function are sparse, we hypothesize that the gross pathology findings of our ovine subjects' renal crest discoloration are likely secondary to prolonged, higher doses of aspirin use. In fact, when we were aware of the mild kidney injuries observed in our 3-month subjects, we immediately reduced the aspirin dose from 81 mg daily to 40 mg daily. In our 6-month subjects, the degree of kidney injury from gross pathology examination is greatly reduced, confirming our hypothesis.

One of the limitations of this study is the ex vivo system's inability to fully simulate the complex left ventricular motion and MV annular dynamics. Additionally, differences exist in normal porcine MV samples and pathologic, degenerative human MV specimens. Our ex vivo MR model only mimics MR due to annular dilation. Furthermore, only rigid and flexible rings are used as commercial controls. Future study should be performed to evaluate the performance of our axis-specific ring in eliminating MR from other etiologies[40], and to compare hemodynamics with other commercial mitral rings with different flexibility and geometry profiles. In our large animal survival experiment, only the axis-specific annuloplasty ring is evaluated, and no rigid or flexible annuloplasty rings were implanted for longer-term evaluation. Though long-term mitral annulus geometry and motion post commercial rigid or flexible annuloplasty ring implantation have been extensively evaluated in human[41] differences may still be present in tissue response and healing in sheep versus in humans, representing another potential limitation. As we continue to move towards commercialization, an immediate next step is to locate a contract manufacturer to upgrade the fabric wrapping for the axis-specific ring to minimize fabric thickness.

In conclusion, an axis-specific mitral annuloplasty ring based on normal human imaging is designed and manufactured to solve two major challenges, allowing for dynamic MV annular conformational changes while restricting the AP dimension. From bench to pre-clinical large animal studies, this axis-specific mitral annuloplasty ring demonstrates sufficient capability to repair MR with excellent chordal force profiles ex vivo, reduces AP dimension and changes in vivo, and allows for dynamic MV annular motion in an ovine large animal model. This axis-specific ring has tremendous potential for direct clinical translatability, representing a promising surgical solution for millions of patients suffering from MR.

Data availability

No existing dataset was used in the study. The source data for Fig. 4 can be found in Supplementary Data 1 and 3. The source data for Fig. 8 can be found in Supplementary Data 1, 4, 5, and 6. The source data for Fig. 8 can be found in Supplementary Data 2. Figures 1–3, 5, and 6 do not have corresponding source data, as they were not required to generate these figures. All other data are available from the corresponding author on reasonable request.

Received: 11 February 2022; Accepted: 28 January 2025;
Published online: 12 February 2025

References

1. De Marchena, E. et al. Respective prevalence of the different Carpentier classes of mitral regurgitation: a stepping stone for future therapeutic research and development. *J. Card. Surg.* **26**, 385–392 (2011).
2. Freed, L. A. et al. Prevalence and clinical outcome of mitral-valve prolapse. *N. Engl. J. Med.* **341**, 1–7 (1999).
3. Singh, J. P. et al. Prevalence and clinical determinants of mitral, tricuspid, and aortic regurgitation (The Framingham Heart Study). *Am. J. Cardiol.* **83**, 897–902 (1999).
4. Nkomo, V. T. et al. Burden of valvular heart diseases: a population-based study. *Lancet* **368**, 1005–1011 (2006).
5. Moore, M., Chen, J., Mallow, P. J. & Rizzo, J. A. The direct health-care burden of valvular heart disease: evidence from US national survey data. *Clin. Outcomes Res.* **8**, 613–627 (2016).
6. Maslow, A. D. & Poppas, A. Primary mitral valve regurgitation: update and review. *Glob. Cardiol. Sci. Pract.* **2017**, e201703 (2017).
7. Grigioni, F., Enriquez-Sarano, M., Zehr, K. J., Bailey, K. R. & Tajik, A. J. Ischemic mitral regurgitation: long-term outcome and prognostic implications with quantitative Doppler assessment. *Circulation* **103**, 1759–1764 (2001).
8. Acker, M. A. et al. Mitral-valve repair versus replacement for severe ischemic mitral regurgitation. *N. Engl. J. Med.* **370**, 23–32 (2014).
9. Wan, S. et al. Mitral valve repair using a semirigid ring: patient selection and early outcomes. *Asian Cardiovasc. Thorac. Ann.* **24**, 647–652 (2016).
10. Ennis, D. B. et al. Changes in mitral annular geometry and dynamics with β-Blockade in patients with degenerative mitral valve disease. *Circ. Cardiovasc. Imaging* **3**, 687–693 (2010).
11. Levack, M. M. et al. Three-dimensional echocardiographic analysis of mitral annular dynamics: implication for annuloplasty selection. *Circulation* **126**, S183-8 (2012).
12. Silberman, S. et al. Repair of ischemic mitral regurgitation: comparison between flexible and rigid annuloplasty rings. *Ann. Thorac. Surg.* **87**, 1721–1727 (2009).
13. Chang, B. C. et al. Long-term clinical results of mitral valvuloplasty using flexible and rigid rings: a prospective and randomized study. *J. Thorac. Cardiovasc. Surg.* **133**, 995–1003 (2007).
14. Jensen, M. O. et al. Saddle-shaped mitral valve annuloplasty rings experience lower forces compared with flat rings. *Circulation* **118**, S250–S255 (2008).
15. Li, B., Young, A. A. & Cowan, B. R. GPU accelerated non-rigid registration for the evaluation of cardiac function. *Med. Image. Comput. Comput. Assist. Interv*. https://doi.org/10.1007/978-3-540-85990-1_106 (2008).
16. Rausch, M. K. et al. Mitral valve annuloplasty: a quantitative clinical and mechanical comparison of different annuloplasty devices. *Ann. Biomed. Eng.* **40**, 750–761 (2012).
17. Imbrie-Moore, A. M. et al. A novel cross-species model of Barlow's disease to biomechanically analyze repair techniques in an ex vivo left heart simulator. *J. Thorac. Cardiovasc. Surg*. https://doi.org/10.1016/j.jtcvs.2020.01.086 (2020).
18. Imbrie-Moore, A. M. et al. Artificial papillary muscle device for off-pump transapical mitral valve repair. *J. Thorac. Cardiovasc. Surg*. https://doi.org/10.1016/j.jtcvs.2020.11.105 (2021).
19. Zhu, Y. et al. Ex vivo analysis of a porcine bicuspid aortic valve and aneurysm disease model. *Ann. Thorac. Surg*. https://doi.org/10.1016/j.athoracsur.2020.05.086 (2020).
20. Zhu, Y. et al. A novel aortic regurgitation model from cusp prolapse with hemodynamic validation using an ex vivo left heart simulator. *J. Cardiovasc. Transl. Res*. https://doi.org/10.1007/s12265-020-10038-z (2020).
21. Zhu, Y. et al. Novel bicuspid aortic valve model with aortic regurgitation for hemodynamic status analysis using an ex vivo simulator. *J. Thorac. Cardiovasc. Surg.* https://doi.org/10.1016/j.jtcvs.2020.06.028 (2020).
22. Paulsen, M. J. et al. Development and ex vivo validation of novel force-sensing neochordae for measuring chordae tendineae tension in the mitral valve apparatus using optical fibers with embedded bragg gratings. *J. Biomech. Eng.* **142**, 0145011–0145019 (2020).
23. Bothe, W. et al. Rigid, complete annuloplasty rings increase anterior mitral leaflet strains in the normal beating ovine heart. *Circulation* **124**, S81–96 (2011).
24. Jensen, M. O. et al. Saddle-shaped mitral valve annuloplasty rings improve leaflet coaptation geometry. *J. Thorac. Cardiovasc. Surg.* **142**, 697–703 (2011).
25. Vergnat, M. et al. Saddle-shape annuloplasty increases mitral leaflet coaptation after repair for flail posterior leaflet. *Ann. Thorac. Surg.* **92**, 797–803 (2011).
26. Padala, M. et al. Saddle shape of the mitral annulus reduces systolic strains on the P2 segment of the posterior mitral leaflet. *Ann. Thorac. Surg.* **88**, 1499–1504 (2009).

27. Jimenez, J. H., Soerensen, D. D., He, Z., He, S. & Yoganathan, A. P. Effects of a saddle shaped annulus on mitral valve function and chordal force distribution: an in vitro study. *Ann. Biomed. Eng.* **31**, 1171–1181 (2003).
28. Vergnat, M. et al. The influence of saddle-shaped annuloplasty on leaflet curvature in patients with ischaemic mitral regurgitation. *Eur. J. Cardio-Thoracic Surg.* **42**, 493–499 (2012).
29. Salgo, I. S. et al. Effect of annular shape on leaflet curvature in reducing mitral leaflet stress. *Circulation* **106**, 711–717 (2002).
30. Okada, Y., Shomura, T., Yamaura, Y. & Yoshikawa, J. Comparison of the Carpentier and Duran prosthetic rings used in mitral reconstruction. *Ann. Thorac. Surg.* **59**, 658–663 (1995).
31. Chee, T., Haston, R., Togo, A. & Raja, S. G. Is a flexible mitral annuloplasty ring superior to a semi-rigid or rigid ring in terms of improvement in symptoms and survival? *Interact. Cardiovasc. Thorac. Surg.* **7**, 477–484 (2008).
32. Timek, T. A. et al. Annular height-to-commissural width ratio of annuloplasty rings in vivo. *Circulation* **112**, I423–I428 (2005).
33. Kaplan, S. R. et al. Three-dimensional echocardiographic assessment of annular shape changes in the normal and regurgitant mitral valve. *Am. Heart J.* **139**, 378–387 (2000).
34. Gorman, J. H., Jackson, B. M., Enomoto, Y. & Gorman, R. C. The effect of regional ischemia on mitral valve annular saddle shape. *Ann. Thorac. Surg.* **77**, 544–548 (2004).
35. Imbrie-Moore, A. M. et al. Ex vivo biomechanical study of apical versus papillary neochord anchoring for mitral regurgitation. *Ann. Thorac. Surg.* **108**, 90–97 (2019).
36. Paulsen, M. J. et al. Mitral chordae tendineae force profile characterization using a posterior ventricular anchoring neochordal repair model for mitral regurgitation in a three-dimensional-printed ex vivo left heart simulator. *Eur. J. Cardiothorac. Surg.* **57**, 535–544 (2020).
37. Pierce, E. L. et al. Mitral annuloplasty ring flexibility preferentially reduces posterior suture forces. *J. Biomech.* **75**, 58–66 (2018).
38. Vahanian, A. et al. 2021 ESC/EACTS Guidelines for the management of valvular heart disease. *G. Ital. Cardiol.* **23**, 1–75 (2022).
39. Lomas, A. L. & Grauer, G. F. The renal effects of NSAIDs in dogs. *J. Am. Anim. Hosp. Assoc.* **51**, 197–203 (2015).
40. Imbrie-Moore, A. M. et al. Ex vivo model of ischemic mitral regurgitation and analysis of adjunctive papillary muscle repair. *Ann. Biomed. Eng.* **49**, 3412–3424 (2021).
41. Nishi, H. et al. Annular dynamics after mitral valve repair with different prosthetic rings: a real-time three-dimensional transesophageal echocardiography study. *Surg. Today* **46**, 1083–1090 (2016).

Acknowledgements

This work was supported by the National Institutes of Health (NIH R01 HL152155 and NIH R01 HL089315-01, Y.J.W.), the Thoracic Surgery Foundation Resident Research Fellowship (Y.Z.), the National Science Foundation Graduate Research Fellowship Program (A.M.I.), and a Stanford Graduate Fellowship (DGE-1656518, A.M.I.). The content is solely the responsibility of the authors and does not necessarily represent the official views of the funders. We would like to thank the generous donation by Donald and Sally O'Neal to support this research effort. We would also like to thank Josh Resnik and Brady Millar for organizing perfusionist coverage to make the in vivo large animal experiments possible.

Author contributions

Y.Z.: conception and design of the work, data acquisition, data analysis, data interpretation, drafting the work. A.I.M.: conception and design of the work, data acquisition, data interpretation, drafting and substantively revising the work. M.H.P.: conception and design of the work, data analysis, data interpretation, substantively revising the work. T.E.C.: design of the work, data acquisition, drafting and substantively revising the work. S.Y.: data acquisition, substantively revising the work. R.J.W.: data acquisition, data analysis, substantively revising the work. N.A.T.: data acquisition, substantively revising the work. M.M.: data acquisition, data interpretation, substantively revising the work. D.M.M.: data acquisition, substantively revising the work. S.W.B.: data acquisition, substantively revising the work. Y.T.: data acquisition, data analysis, substantively revising the work. M.L.: data analysis, substantively revising the work. V.Y.W.: data analysis, substantively revising the work. S.E.: data acquisition, substantively revising the work. S.M.: data acquisition, substantively revising the work. S.A.: data acquisition, substantively revising the work. S.K.W.: data acquisition, substantively revising the work. H.J.L.: data acquisition, substantively revising the work. C.H.: data analysis, substantively revising the work. K.M.: data acquisition, substantively revising the work. O.S.K.: data acquisition, substantively revising the work. J.M.: data acquisition, substantively revising the work. Y.S.: data acquisition, data interpretation, substantively revising the work. D.B.E.: design of the work, data interpretation, substantively revising the work. Y.J.W.: conception and design of the work, data interpretation, substantively revising the work. All authors have approved the submitted version of the manuscript.

Competing interests

The authors declare the following competing interests: Y.J.W., Y.Z., A.M.I.-M., M.H.P., and M.J.P. filed a provisional US patent (application number 18/094,213) and PCT application (application number PCT/US21/41803). The device design and manufacturing are covered in patent application.

Additional information

Supplementary information The online version contains supplementary material available at https://doi.org/10.1038/s43856-025-00753-6.

Correspondence and requests for materials should be addressed to Y. Joseph Woo.

Peer review information *Communications Medicine* thanks John Carney, Mohammed Alaa Omar, and Soeren Skov for their contribution to the peer review of this work. Peer reviewer reports are available.